Solid-State Synthesis of Phase-Pure Micron-Sized Patrónite Vanadium Tetrasulfide toward Practical Magnesium Batteries

Adam Reupert, Hanna Schleicher, Yang Hu,* Stefan Fuchs, Manuel Dillenz, Camelia N. Borca, Thomas Huthwelker, Axel Groß, Maximilian Fichtner,* and Zhenyou Li*

The Patrónite vanadium tetrasulfide (VS_4) follows a simultaneous cationic and anionic redox (SCAR) mechanism in magnesium batteries, which renders a delocalized electronic structure for fast kinetics and meanwhile enables multi-electron reactions for delivering high capacity. In contrast to most research that focuses on the hydrothermal route resulting in VS_4 nanoparticles, herein a more industrially relevant synthesis route is targeted, utilizing a solid-state approach leading to micron-sized VS_4. The obtained $2 \times 10\,\mu m$ VS_4 needles show good water/air stability, allowing an environmentally friendly coatings procedure using polyvinylpyrrolidon binder in isopropanol. Electrochemical investigation shows that the micron-sized VS_4 cathode delivers a maximum capacity of $420\,mAh\,g^{-1}$ in a tetrakis(hexafluoroisopropyloxy)borate ($Mg[B(hfip)_4]_2$)-based electrolyte, however suffers from fast capacity fading and overcharging. Targeting these issues, a concentrated $Mg[B(hfip)_4]_2$ electrolyte in bis(2-methoxyethyl)ether is applied, which enables stable cycling for 300 cycles at the expense of a reduced capacity. Multimodal characterizations confirm a reversible SCAR mechanism of VS_4 during cycling. However, pulverization of the electrode and fragmentation of the VS_4 backbones are evident, leading to the leakage of active material into electrolyte and causing capacity decay. To avoid active material loss, crystal engineering or surface protection strategies should be developed toward practical Mg batteries.

1. Introduction

Research interest in energy storage devices increased drastically over the last few decades. Of particular interest in this matter are batteries as they have the ability to store and provide electrical energy on demand by utilizing reversible electrochemical processes with high efficiency. The ongoing electrification of the vehicle sector as well as the rising demand for energy storage solutions regarding renewable energy sources is recently added on top of the already established market of portable devices like laptops and mobile phones.[1,2] As the growing market requires more resources to satisfy this need and the current solutions rely on partially critical materials, alternative battery solutions are in demand.

Beyond lithium batteries address the resource criticality by utilizing more sustainable and often less toxic or safer battery chemistries than the current generation of batteries.[3,4] Multivalent batteries, one section of beyond lithium batteries, feature the advantage of transporting more than one charge per ion. In the case of magnesium,

A. Reupert, H. Schleicher, Y. Hu, S. Fuchs, M. Fichtner, Z. Li
Helmholtz Institute Ulm (HIU) Electrochemical Energy Storage
Helmholtzstraße 11, 89081 Ulm, Germany
E-mail: yang.hu@kit.edu; m.fichtner@kit.edu; lizhenyou@qibebt.ac.cn

A. Reupert, H. Schleicher
Institute for Inorganic Chemistry II
Ulm University
Albert-Einstein-Allee 11, 89081 Ulm, Germany

Y. Hu, S. Fuchs, M. Fichtner
Institute of Nanotechnology (INT)
Karlsruhe Institute of Technology (KIT)
P.O. Box 3640, 76021 Karlsruhe, Germany

M. Dillenz, A. Groß
Institute for Theoretical Chemistry
Ulm University
Oberberghof 7, 89081 Ulm, Germany

C. N. Borca, T. Huthwelker
Swiss Light Source
Paul Scherrer Institute (PSI)
Forschungsstrasse 111, 5232 Villigen, Switzerland

Z. Li
Qingdao New Energy Shandong Laboratory
Qingdao Institute of Bioenergy and Bioprocess Technology
Chinese Academy of Sciences
No. 189 Songling Road, Laoshan District, Qingdao 266101, China

the double-charged ion allows for the transference of up to two electrons per ion leading to an almost doubled volumetric capacity compared with metallic lithium (2046 vs 3833 mAh cm^{-3}).[5,6] Calculation of diffusion barriers showed that magnesium can have a dendrite-free deposition, which in contrast to lithium, enables the usage of a metal anode.[6] However, owing to their higher charge, Mg^{2+} possesses a smaller effective ionic radius, even smaller than Li$^+$ (90 pm vs 86 pm for a sixfold coordination number).[7] This leads to a high charge density of the ion causing strong coulombic interactions within a host lattice thus resulting in a high energy barrier lowering the diffusion kinetics even further.[8,9] To decrease migration barriers, transition metal sulfides (TMSs) and selenides are regarded as promising as they provide a softer framework compared to their oxidic counterpart.[10] Nevertheless, even the TMS compounds generally suffer from kinetic hindrance upon Mg^{2+} insertion, with their cycling performance strongly dependent on the size of the active particles.[11] To the best of our knowledge, the Chevrel phase (CP) Mo$_6$S$_8$ is almost the only material that enables fair Mg^{2+} de-/insertion kinetics at room temperature with micron-sized particles.[12]

While conventional material design principles and kinetic improvement strategies developed for monovalent systems can be hardly transferred to Mg batteries, unconventional approaches were proposed and attracted increasing interest in the community.[13,14] One concept to mitigate the diffusion barrier is the utilization of materials that are capable of simultaneous cationic and anionic redox processes (SCAR concept). By selecting materials with a strong p–d band orbital overlap, not only the transition metal but also the anionic part gets oxidized and reduced during de-/insertion resulting in a flexible environment regarding electron transfer processes.[15,16] This beneficial distribution of delocalized electrons is sometimes also acquired by metal clusters as in the case of the well-explored CP Mo$_6$S$_8$, the current magnesium benchmark cathode material.[9,12,17] Sulfide and selenide compounds of early d-block elements (group 4–6) are extensively studied as potential multivalent cathode materials as they can fulfill the requirements of overlapping d- and p-states and are comparably cheap while showing good initial cycling performance.[9,10,12,16,18–22] Among them, vanadium sulfides (VS$_2$ and VS$_4$) are of particular interest, as the vanadium metal features a rather flexible valence structure by up to five different possible oxidation states. Furthermore, calculations showed that the energies of the vanadium d-states and the p-states of sulfur are almost identical, creating an ideal candidate to investigate the SCAR principle.[9,19]

VS$_4$ appears in a monoclinic crystal structure indexed with space group C2/c consisting of individual quasi-1D VS$_4$ ribbons (see **Figure 1**). Each ribbon consists of vanadium (V^{4+}) bridged by two disulfide S$_2^{2-}$ groups. The individual strings are arranged alongside each other, held only by weak van der Waals interaction.[23] Insertion of magnesium and diffusion within the material is proposed to appear by a hopping from disulfide to disulfide group along the ribbons, causing a partial reduction of the disulfide groups to individual S^{2-} and an internal oxidation of vanadium from +IV to +V.[24] The unique charge storage mechanism renders a significantly improved capacity (theoretical capacity 448 vs 122 mAh g^{-1}) and C-rate compared to the CP Mo$_6$S$_8$.[24,25]

A recent review article from Liu et al. covering exclusively vanadium sulfides (VS$_2$ and VS$_4$) shows the high research interest of this material class while also summarizing that the vast majority of VS$_4$ is currently produced hydrothermally.[26] The solid-state synthesis approach to synthesize VS$_4$ was investigated only sparingly, covered in just a few articles. This probably developed from the size difference of the obtained VS$_4$ particles. A solid-state reaction usually results in larger particle sizes than the particles obtained by a hydrothermal approach. The obtained VS$_4$ nanoparticles were favored as the larger surface area and smaller size lowered bulk diffusion and volume expansion when utilized as storage material and therefore typically resulted in higher C-rates, capacities, and easier processability.[26] On the other hand, nanosized materials show higher reactivity, which could be disadvantageous as they could facilitate parasitic reactions.

A recent report from Qin et al. discusses the importance of the development of a solid-state synthesis of VS$_4$ as there are several upscalability issues with the current hydrothermal approach.[27]
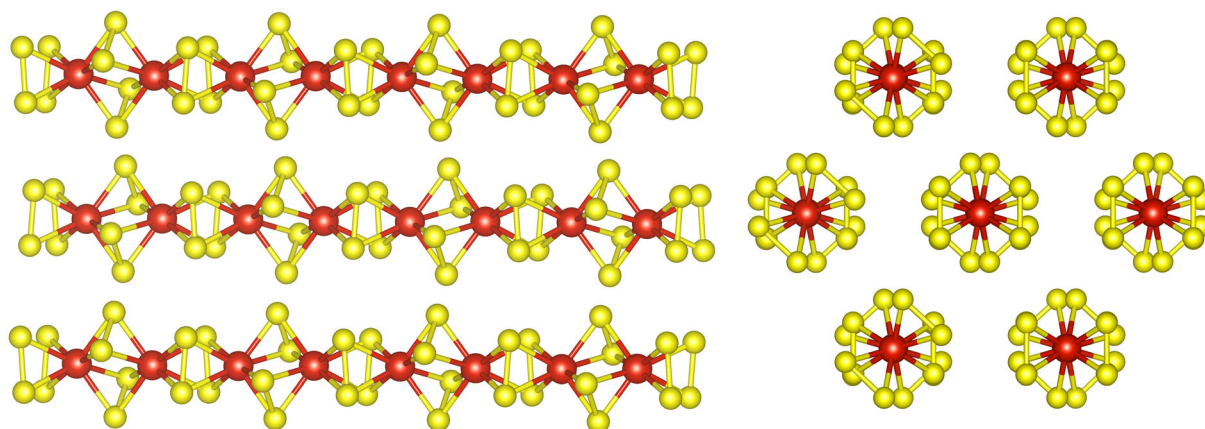
Figure 1. Visualization of the chain-like structure of VS$_4$. On the left side, individual VS$_4$ ribbons of the monoclinic structure are displayed. On the right side, a top-down perspective of the ribbons is displayed, highlighting that the individual ribbons are only held together by van der Waals forces and no molecular bond bridging. The structural representation is drawn utilizing the VESTA software and a refined crystallographic information file (cif) obtained from the FullProf Suite.[80,81] The respective refinement can be found in the supporting information, see Figure S7, Supporting Information.

VS_4 is an ideal candidate for early pilot projects to show the viability of magnesium batteries. However, to produce larger amounts of active material, more industrial-relevant approaches have to be investigated.

Furthermore, quenching and doping by the solid-state approach are viable options to alternate the micron-sized morphology of VS_4, which are currently completely unexplored.

To advance in this direction, a reliable and systematic investigation of easy upscalable methods is necessary.

A recent theoretical study regarding the insertion mechanism of Mg into VS_4 suggests a more complex behavior, presumably resulting in magnesium clustering within the host lattice leading to unstable phase formation and possible degradation.[28] Experimentally, VS_4 investigations predominantly rely on nanosized material (hydrothermal synthesis) to further shorten diffusion paths within the active material particles enabling higher C-rates and capacities.[26] However, rapid capacity decay, a sensitive hydrothermal synthesis, and its amorphous nature often hinder a detailed systematic investigation and further upscalability of this material.[29]

A multitude of approaches for the nanosized VS_4 is investigated to improve the cycling stability and rate capability of VS_4. This includes doping, coating, lattice expansion, the fixation of VS_4 on substrates, synthesis of specific morphologies to increase the particle surface area, the generation of anchoring sites, and many more.[29–33] Investigations focusing on larger particle systems tried to increase the low rate performance by growing 1 µm VS_4 particles onto a Ti_3C_2/C surface, obtaining a stable capacity of 180 mAh g^{-1} at 500 mA g^{-1} ($\approx$1 C) utilizing a chlorine-based electrolyte.[30] Thereby, $MgCl^+$ cations were diffusing within the VS_4 cathode material, possessing a lower diffusion barrier in the cathode material, potentially being an effective way to circumvent ion clustering within the cathode material. Other reports that modified the electrolyte to lower the cation diffusion barrier in the cathode material investigated co-insertion by utilizing a dual salt electrolyte consisting of a monovalent and multivalent electrolyte composition. In this case, the monovalent ion is supposed to occupy unused sites and/or to expand the layers of the crystal, lowering coulombic interactions and enhancing the diffusion of the multivalent species within the material.[8,33] Another approach to stabilize VS_4 is by using doping agents. Small amounts of phosphorous and molybdenum showed improvements regarding cycling stability.[34,35] In the case of the Mo-dopant, this was attributed to the introduction of sulfur vacancies and interlayer expansion. Modifications in this direction could offer an interesting strategy to mitigate magnesium clustering lowering the degradation of the active material.[28,34]

A comparison of nano- and microsphered VS_4 particles regarding capacity and rate performance showed significantly lowered capacity for micron-sized particles ($\approx$50 mAh g^{-1}) versus nanosized VS_4 (100 mAh g^{-1}). Nevertheless, both materials showed fast capacity fading.[32] The report attributed insufficient electronic conductivity as the root cause and stabilized the material using carbon nanotubes to obtain capacities around 200 mAh g^{-1}.[32] Unfortunately, the article did not cover the performance of micron-sized VS_4 attached to carbon nanotubes and only compared to the unoptimized micron-sized particles showing low capacities below 50 mAh g^{-1}. Li et al. discussed the morphology-dependent electrochemical performance of VS_4 and other comparable cathode materials.[36] They highlighted that micron-sized VS_4 is neglected in current research although comparable systems (MoS_2) showed the importance of designing particles with a special micro–nano size morphology, reaching higher decomposition temperatures, larger capacity derived from enhanced ion diffusion, and potential higher cycling stability. In their article, they looked at three different surface morphologies of VS_4 spheres and were able to modify the capacity and cycling stability with these modifications.[36]

Since most reports only investigate improvements of the nanosized VS_4 material, researching the kinetic behavior, storage mechanism, and degradation mechanism of micron-sized VS_4 in Mg batteries and therefore creating a baseline for further upscalable research attempts are of significant practical importance. A recently published perspective article proposed a strategy to achieve 160 Wh kg^{-1} (cell level) Mg battery by employing a 11.8 mg cm^{-2} VS_4 cathode.[12,37] To achieve such high mass loading, micron-sized particles are beneficial.

Motivated by the abovementioned findings, this work targets a more industry driven, easy upscalable and modifiable solid-state process to obtain phase-pure VS_4.[27] As a side effect, micron-sized needle-like particles were obtained, requiring a stepwise refinement of postprocessing, slurry coating, and electrolyte formulation. Parameter refinements of the solid-state reaction were monitored by X-ray diffraction (XRD) measurements of the products. Morphological and compositional analysis was performed by scanning electron microscopy (SEM) and energy-dispersive X-ray spectroscopy (EDX) analysis. The influence of postprocessing on the particle size was evaluated by dynamic light scattering (DLS) measurements. A closer characterization of the successfully synthesized VS_4 was achieved utilizing Rietveld refinement, pair distribution function analysis (PDF), X-ray absorption near edge spectroscopy (XANES), X-ray photoelectron spectra (XPS), and Raman and Fourier-transform infrared spectroscopy (FT-IR). The XANES measurements were thereby supported by periodic density functional theory (DFT) calculations. The resultant phase-pure, micron-sized VS_4 was subject to electrochemical investigation in Mg batteries using Mg tetrakis(hexafluoroisopropyloxy)borate-based ($Mg[B(hfip)_4]_2$.3DME) electrolyte. The electrolyte formulation was optimized by concentration (0.1, 0.3, and 0.5 M) and solvent variation, utilizing dimethoxyethane (DME), bis(2-methoxyethyl)ether (G2), and tetraethylenglycoldimethylether (G4). Coating properties were adjusted to achieve good slurry formation and blade coating with alternative binders that do not require the use of toxic N-methyl-2-pyrrolidone (NMP). Ex situ studies to investigate the charge storage as well as degradation mechanisms were performed by XANES and XPS studies.

2. Results and Discussion

2.1. Solid-State Synthesis of VS$_4$

The solid-state approach was explored utilizing the elemental precursors vanadium metal (V) and sulfur (S_8). However, synthesis approaches using V_5S_8 as a precursor were also successful

(Figure S1, Supporting Information). To test for trends in the synthesis step, all parameters except one were varied. Figure S2, Supporting Information, shows that VS$_4$ could be successfully synthesized in all cases. Remains of sulfur were effectively removed during the CS$_2$ washing step, as no remaining S$_8$ reflexes were seen in the VS$_4$ diffractograms.

A noncomplete reaction can be observed in Figure S2a, Supporting Information, as the strongest V-metal reflex arising from the educt around 15° 2θ appeared in all patterns. Increased sulfur led to a decreased vanadium side phase. To balance between the produced VS$_4$ per ampoule batch and a lower V-metal side phase, the one to six ratio was fixed and milled at different ball milling speeds. Choosing the 1:6 over the 1:8 ratio also lowers the amount of unreacted sulfur, which has to be removed in the subsequent washing steps. Figure S2b, Supporting Information, shows that the ball milling speed had a drastic effect on the purity of the produced VS$_4$. Monitoring of the phase purity was again performed by close inspection of residual reflections arising from the vanadium metal educt, in particular the main reflex at 15°. An increased mixing speed lowered the vanadium side phase significantly. At ball milling speeds of 250 and 500 rpm, the material stuck to the ball mill container and had to be scraped manually every few cycles leading to worse mixing compared to the higher speeds where caking did not occur anymore. This result surprised as the heating conditions of the solid-state synthesis were performed at temperatures where sulfur occurs in a molten state and contact issues between sulfur and vanadium should not be an issue. XRD results of the milled compounds (Figure S3, Supporting Information) also excluded the possibility of a mechanochemical reaction. We can therefore attribute the improved yield and purity to the formation of smaller vanadium particles during the more intense mixing step. As 750 rpm showed the lowest amount of impurities, this speed was fixed and milling times for multiple durations were tested. Figure S2c, Supporting Information, displays that ball milling beyond 2 h of milling time had no observable vanadium metal side phases anymore, leading to phase-pure VS$_4$. The heating step led to an incomplete reaction to VS$_4$ for temperatures below 400 °C (Figure S2d, Supporting Information) or reaction times shorter than 48 h (Figure S2e, Supporting Information). To minimize pressure build-up within the ampoules due to the low boiling point of sulfur (445 °C) and because previous reports mention a decomposition of VS$_4$ to V$_5$S$_8$ above 450 °C, a temperature range of 400–445 °C for at least 48 h was identified as ideal to synthesize VS$_4$.[38]

By applying a 1 to 6 (V:S) ratio with a milling speed of 750 rpm for 5 h and a reaction time of 60 h at 400 °C, multiple batches of phase-pure VS$_4$ were synthesized and washed with CS$_2$ (Figure S4, Supporting Information). After confirmation of the successful synthesis with XRD, all batches were mixed together and characterized in more detail.

SEM images depicted in **Figure 2**a showed large agglomerates, ranging between 20 and 100 μm in size. At higher magnification (Figure 2b,d), the characteristic needle shape of VS$_4$ was observable. Large particles caused by agglomeration were not desirable as they lead to inhomogeneous coating and poor rate performance during cycling, as more bulk diffusion is required. Additionally, unreliable electrochemical performance was observed as sulfur could be trapped in those particles boosting the capacity uncontrollably, sometimes even above the theoretical capacity of pure VS$_4$ (Figure S5, Supporting Information).

To eliminate capacity contribution of trapped sulfur and to obtain a reduced, more uniform size distribution, a postprocessing milling step was added. Initial dry milling attempts resulted in amorphization and phase changes and were replaced by a wet milling approach (Figure S6, Supporting Information). Isopropanol was reported to show the best dispersion properties and was used for solvent-assisted ball milling.[39] A reduction in size could be seen (Figure 2a,c) in the SEM images and was experimentally measured using DLS (Figure 2e). The milling step lowered the average particle size drastically by reducing agglomerates and increasing the amount of individual primary particles. An additional CS$_2$ washing step removed the accessible residual sulfur and the so processed Patrónite showed reasonable and reproducible electrochemical performance during cycling.

2.2. Characterization of Micron-Sized VS$_4$

To gain more insight into the overall material properties, the synthesized, ball-milled, and CS$_2$-washed material was thoroughly
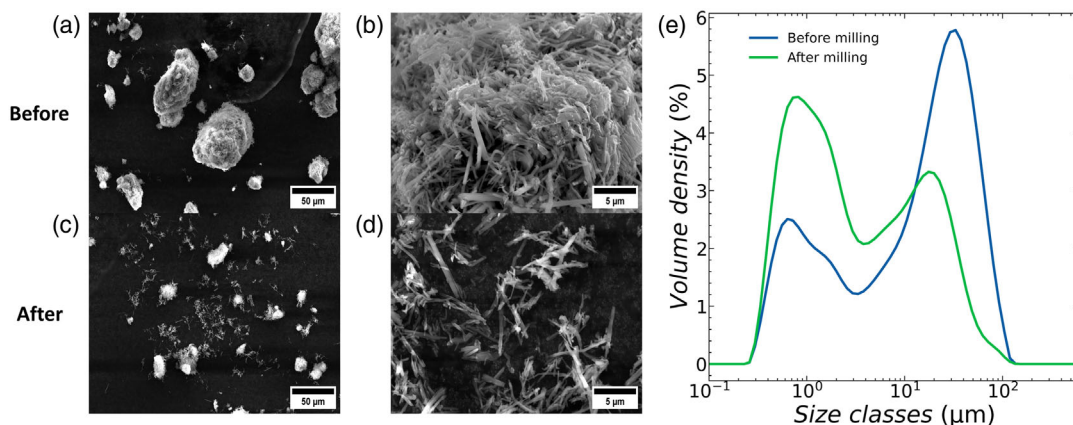
Figure 2. SEM images of VS$_4$ a) before and c) after an applied postprocessing step by wet milling. b,d) A zoomed image of the particle surface before and after the treatment, respectively. DLS measurement for size comparison of obtained VS$_4$ particles is shown in e).

characterized. The crystal structure of VS_4 was further examined by Rietveld refinement (Figure S7a, Supporting Information) assuming a monoclinic C2/c space group. Structure parameters from the Rietveld refinement as well as lattice parameters of a relaxed crystal structure obtained from DFT calculations, shown in Table S1, Supporting Information, are in line and in good agreement with the literature.[20,40] Comparison of the radial distribution accessed by PDF (displayed in Figure S7b, Supporting Information) with a calculated pattern from the crystal file obtained by Rietveld refinement matched well and showed all important atomic distances. The disulfide distances appear around 2.0 Å, while the most prominent signal from 2.4 to 2.5 Å is related to V–S distances. The V–V distances could be observed at 2.8 and 3.2 Å.

The Raman modes (Figure S8a, Supporting Information) match well with calculated and experimental values for VS_4 from the literature.[23,24,41] Thereby, the first two signals at 200 and 221 cm^{-1} can be attributed to a V–S stretching mode. The modes at 271, 286, 543, and 556 cm^{-1} are attributed to the disulfide group, where the first two represent the S–S stretching and the latter two are from the S–S twisting mode. The strongest band at 347 cm^{-1} represents V_2S_4 cage breathing. FT-IR results (Figure S8b, Supporting Information) show transmittance at 545 cm^{-1} that can be attributed to the V–S–V stretching of the disulfide group, while the signal at 968 cm^{-1} represents terminal V=S stretching. According to the literature, the signal at 1118 cm^{-1} can be attributed to the stretching vibration of a sulfite group, while the slight peak at 1400 cm^{-1} arises from a sulfate group, indicating slight oxidation of VS_4 in air atmosphere.[42–44] The weak signal around 1600 cm^{-1} can be attributed to the scissor bending of absorbed water from handling the samples in air.[45,46]

Figure 3a,b shows the normalized S and V K-edge XANES in comparison with selected standards of the nominal composition of $Ti^{4+}S_2^{2-}$, $V_4^{3+}V^{4+}S_8^{2-}$, $Ca^{2+}S^{6+}O_4^{2-}$, $V^{2+}O^{2-}$, $V_2^{3+}O_3^{2-}$, $V^{4+}O_2^{2-}$, and $V_2^{5+}O_5^{2-}$. Pristine VS_4 has a chain-like molecular structure composed of V^{4+} ions coordinated to sulfur dimers (S_2^{2-}). For the S K-edge (Figure 3a), the whitelines of VS_4 around 2471.5 eV matched the energy position expected for the S_2^{2-} group, which were close to that of a V_5S_8 reference and slightly higher than TiS_2, in which the formal oxidation of sulfur in TiS_2 might deviate significantly from the nominal composition ($Ti^{4+}S_2^{2-}$) due to the covalent bonds between Ti and sulfur (e.g., $Ti^{2.7+}S_2^{1.35-}$).[47,48] Both V_5S_8 and TiS_2 also showed a splitting of the whiteline that can be explained by multiple inequivalent crystallographic S^{2-} sites. For VS_4, the broad band close to 2479 eV was considered from the multiple-electron scattering, which was lower in energy compared with a $CaSO_4$ reference ($\approx$2482.5 eV). The V K-edge of pristine VS_4 (Figure 3b) shows multiple pre-edge and shoulder-like features; the former reflected the quadrupole $1s \rightarrow 3d$ transition.[20] It is worth noting that the pristine VS_4 powder, as-prepared electrode and the electrode at OCV state (resting for 48 h) demonstrated distinct whiteline intensity in S K-edge and showed a slight variation in V pre-edge features, which might result from the different over absorption between the diluted pellet and casted electrode tapes.

The XANES spectra obtained from DFT calculations based on the excited electron and core–hole (XCH) method showed good qualitative agreement. Thus, all features of the experimentally measured VS_4 (Figure 3c,d) are well reflected while minor deviations in peak intensity and broadening are observed. The calculated density of states (DOS, Figure 3e) displays strong hybridization of the vanadium d- and sulfur p-states, indicating the prevalence of covalent bonds in the structure. This is in line with the observed contributions of both, vanadium and sulfur redox activity, proofing that VS_4 belongs to the class of SCAR materials, which is capable of undergoing simultaneous cationic and anionic redox during cycling.

Surface investigations, performed by XPS (Figure 3f), distinguished multiple oxidation states for vanadium between +II and +IV. In the sulfur S $2p$ spectra, we can see signals from the disulfide group, elemental sulfur, sulfite, and a minor contribution of sulfate. Thereby, the fitted peaks in the S $2p$ spectra strongly overlap, as the peak separation of the $p_{1/2}$ and $p_{3/2}$ is in the same range of binding energy shifts derived through the different sulfur oxidation states. Except for the disulfide and the V^{4+} signal, all other species can be seen as purely surface defects formed on handling the substance in air. Major phase formation can be excluded as no other bulk techniques showed those side phases. Only the sulfite group is in accordance with previous measurements as it could also be measured as a weak signal in the FT-IR and XANES measurements.

2.3. Coating Investigation

The active material VS_4 can be synthesized using a water-based hydrothermal route and is found in nature as the mineral Patrónite. To further study the air and water stability of this material, XRD measurements of VS_4 were repeated after exposure of the material to air and water for several days, which showed no alternation of the structure (Figure S9, Supporting Information). Additional stability tests were carried out by adding VS_4 to water in basic conditions (pH = 10, utilizing NaOH) and acidic conditions (pH = 5, utilizing HCl). After 3 days, the material under basic conditions degraded, releasing a characteristic H_2S smell and showed a slight dark discoloration of the aqueous phase, while the material in the acidic environment was not showing any color changes or odor. This should allow water-based processing in neutral to slight acidic conditions leading to more sustainable and less toxic slurry preparations. In contrast to most reports which use VS_4 in combination with toxic polyvinylidene fluoride (PVDF)/N-methyl-2-pyrrolidone (NMP) binder solutions, we focused on NMP solvent-free slurries starting with water-soluble carboxymethyl cellulose (CMC)/styrene-butadiene rubber (SBR) binder. Those slurries showed a tendency to segregate the VS_4 from the water leading to inhomogeneous coatings, which was surprising as previous studies used this combination for their slurry coating of VS_4.[49,50] To avoid this segregation, the dispersibility of VS_4 with H_2O/IprOH mixtures was tested. Figure S10, Supporting Information, vial B shows how VS_4 crawled up the vial walls to minimize water contact because of the strong hydrophobic nature. A good dispersibility could be reached in isopropanol or mixtures containing isopropanol (Figure S10, Supporting Information; vial A and C), with mass fractions of IprOH above 40 wt%. Although we were able to successfully coat VS_4 with the mentioned solvent mixture (Figure S11, Supporting Information), CMC was not dissolved
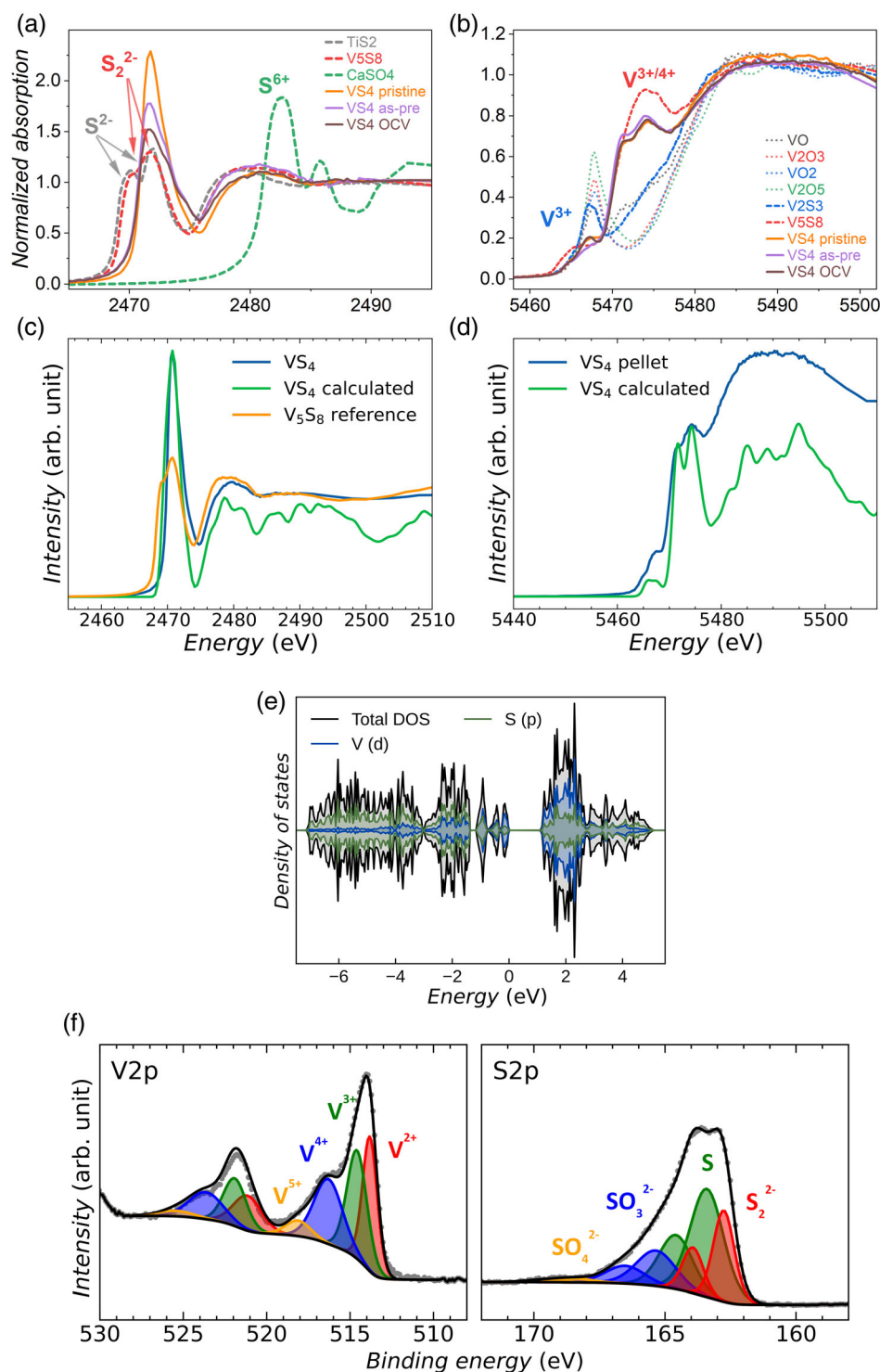
Figure 3. Normalized a) S and b) V K-edge XANES for pristine VS$_4$ (pellet form), as-prepared VS$_4$ electrode, and VS$_4$ in a half-cell at OCV. Corresponding theoretical calculations from DFT are displayed in plot c–e), while XPS results of the pristine material are shown for the V and S region in subfigure f).

completely in those isopropanol mixtures, always remaining slightly translucent. This resulted in an opposing effect as a higher concentration of isopropanol improved the dispersion properties of VS$_4$ but lowered the dissolution of CMC drastically

and in extreme concentrations led to nonreversible polymerization reactions that formed plastic-like precipitations of the polymer. Handling those solutions turned out to be tricky so after multiple unsatisfying attempts, the slurry processing was

**ADVANCED
SCIENCE NEWS**

www.advancedsciencenews.com

**small
structures**

www.small-structures.com

changed to a water-free polyvinylpyrrolidone (PVP)/isopropopanol binder mixture. This improved the coating quality considerably, achieving uniform, well-dispersed VS_4 slurries, and coatings.

2.4. Electrochemical Study

Galvanostatic cycling with potential limitation measurements of VS_4 (**Figure 4**a) between 0.01 and 2.7 V versus Mg/Mg^{2+} with a 0.3 M $Mg[B(hfip)_4]_2$.3DME electrolyte in DME showed a fast activation of the active material, reaching a peak capacity of 420 mAh g^{-1}, close to the theoretical value, within 10 cycles. Considering the current applied (50 mA g^{-1}) and particle size of the active material, the result indicates a fair Mg^{2+} diffusion kinetics in the VS_4 bulk. However, a fast capacity fading appeared after reaching peak capacity, accompanied by severe overcharge. From cycle 40 onward, the capacity dropped below 100 mAh g^{-1}. To address the overcharging and fading, which we assumed was

related to dissolution of active material, magnesium trapping in the cathode material, and decomposition products like anode passivation by polysulfide shuttling, we varied the cutoff voltages and electrolyte formulations regarding solvent and concentration.[28] Utilization of higher glyme types and concentrations targeted toward limitation or even suppression of active material dissolution. These strategies are known to act beneficial in conventional metal sulfur batteries to mitigate polysulfide shuttling and were tested with the same motivations in the Mg||VS_4 cells.[51]

An increase of the salt concentration (Figure 4b) to 0.5 M delayed the activation but also degradation and lowered the maximum capacity to 220 mAh g^{-1}. Compared to the 0.3 M concentration, the overcharge is moderate. Further increase of salt concentration to 0.7 M showed a positive effect as further reduction of overcharge was observed, while the maximum capacity of 220 mAh g^{-1} remained unaltered. Unfortunately, the overall cycling performance was not stable and multiple cells failed, which could be related to an oversaturation of the electrolyte solution as the concentration was reaching the solubility limit during preparation and had to be filtered before usage. A change of the electrolyte solvent from DME to higher glymes (G2 and G4) at a fixed concentration (0.3 M) showed a reduction of overcharging. Unfortunately, the higher glymes were also increasing the overpotentials during cycling and therefore lowered the capacity (Figure S12, Supporting Information). In the case of G4, multiple cells were directly reaching the cutoff voltages and could not be cycled. Other cells showed a delayed activation that would contribute to the highly increased viscosity of G4 in comparison with the lower glymes and therefore a prolonged wetting time of the electrodes after assembly. Another reason can be the difference in solvation energy interaction of the solvent with the electrolyte in particular with the magnesium cations. The limits of electrolyte concentration and chosen glyme type were also directly reflected in the coulombic efficiency as strong fluctuation is apparent in these cells. The mentioned difficulties resulted in multiple cycles, where no clean charge/discharge profiles were obtained as the overpotentials strongly varied during cycling as well as some potential spikes could be observed. We therefore settled on the 0.5 M concentration with G2 as solvent and checked different cutoff voltages. In almost all literature, reports about VS_4 as active material for magnesium batteries that showed semistable cycling, chose cutoff potentials below 2.5 V.[29,36] We initially related this to the common use of chlorine-based electrolytes in magnesium batteries with the inherited reduced stability window of those electrolytes and also the ability of chlorine to lower the overpotential rendering higher cutoff voltages unnecessary. Tests to keep the potential at 2.7 V for longer time periods led to the complete failure of multiple coin cell batteries showing that this voltage is also unsuited for chlorine-free glyme-based electrolytes as it is outside the stability window of VS_4. Repetition of the same tests for 2.5 V showed no stability issues within the same time frame. The most prominent change of the reduced upper limit of 2.5 V was the further reduction of the maximum capacity to only one-fourth of the theoretical capacity (0.5 M/G2). On the other side, overcharging was further reduced leading to increased coulombic efficiencies of around 94% and stable cycling for over 300 cycles. A decrease of the upper cutoff potential, lower than 2.5 V, or an increase of the lower cutoff to
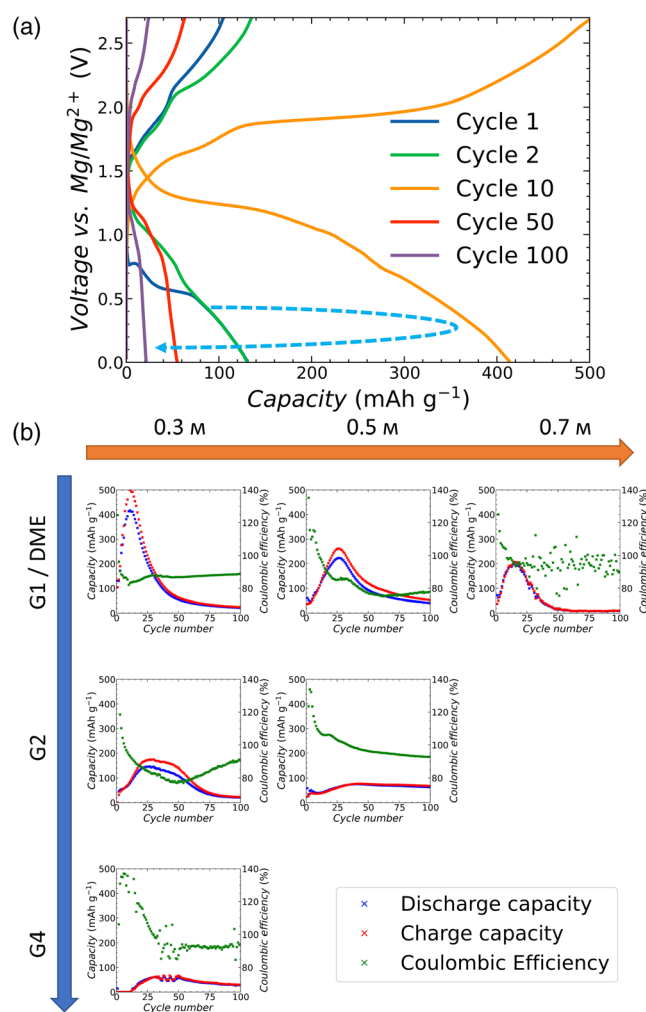
Figure 4. a) Galvanostatic cycling profile of VS_4 between 0.01 and 2.7 V versus Mg/Mg^{2+} using 0.3 M $Mg[B(hfip)_4]_2$ electrolyte in DME and a current of 50 mA g^{-1} ($\approx$0.1 C). b) Capacity versus cycle number plots are displayed with varying salt concentrations and solvent types. 0.5 M/G2 shows the most stable cycling performance for the borate-based electrolyte.

0.5 V or higher strongly reduced the capacity and did not help to reduce overcharging issues.

The sulfuric nature of the cathode material restricts the choices for electrolytes to only non-nucleophilic options. Cycling tests with other, conventional, Mg-electrolytes like $Mg(HMDS)_2$-$2AlCl_3$ in THF (or DME) and Grignard-based reagents like MeMgCl in THF showed only initial discharge capacity and could not be recharged and were therefore not cyclable.

As the herein used $Mg[B(hfip)_4]_2$ electrolyte salt is not commercially available and requires a complete air/moisture-free atmosphere during synthesis, scale-up of this component might be challenging if VS_4 will be tested in a pilot project. One viable option for an easier obtainable electrolyte salt might be magnesium trifluoromethanesulfonate $(Mg(CF_3SO_3)_2)$. However, the comparability and cycling performance of this electrolyte with VS4 has to be tested.

2.5. Charge Storage and Degradation Mechanisms

All mechanistic investigations were performed utilizing the 0.3 M $Mg[B(hfip)_4]_2$ electrolyte as degradation characteristics were more apparent and easier to identify and track. An increase in electrolyte concentration or a switch to higher glymes should only lower the severity but not the degradation mechanism. To check for possible degradation pathways, a cell was disassembled after 500 h of resting at open circuit voltage (OCV, **Figure 5**a left side). The voltage dropped during the OCV measurement from 1.8 to 1.1 V suggesting a slow self-discharge of the cell. To minimize this effect, later coin cells were started cycling, with a maximum resting time of 0–2 h after the cell assembly. The separators showed dark spots indicating detached material from the electrode coating and successive traveling of the material towards the anode. A closer investigation of the VS_4 coating by SEM imaging revealed cracking of the electrode, hinting toward strong volume changes and possible pulverization of the material. This is not observed for the pristine coatings before assembly nor for samples that were submerged in DME overnight as they showed completely uniform coatings (Figure S13, Supporting Information). Cycling of VS_4 within a flooded cell (Figure 5a, right side) showed a strong discoloration of the transparent electrolyte to dark gray/violet. After a longer time, small particles started to sediment from the liquid indicating a pulverization of the active material during cycling. In agreement with our observations, Kozlova et al. reported the appearance of a violet color for finely colloidal dispersed VS_4 particles.[39] Subsequent Raman measurements of the discolored electrolyte could only detect signals arising from VS_4. Magnesium polysulfide species could not be measured by Raman, thus a simple polysulfide shuttling, like in the case of magnesium sulfur cells, seems not to occur. This agrees with the literature, where VS_4 is used as separator coating in metal sulfur cells to serve as anchoring sites to trap polysulfide species.[52]

Considering a recent publication by Jankowski and Lastra that utilized DFT calculations to investigate magnesium diffusion within the VS_4 material, we assume, as the proposed cycling profiles are in good agreement with ours, that the main degradation of the material stems from the uneven diffusion within the material.[28] This leads to magnesium clustering that then leads to
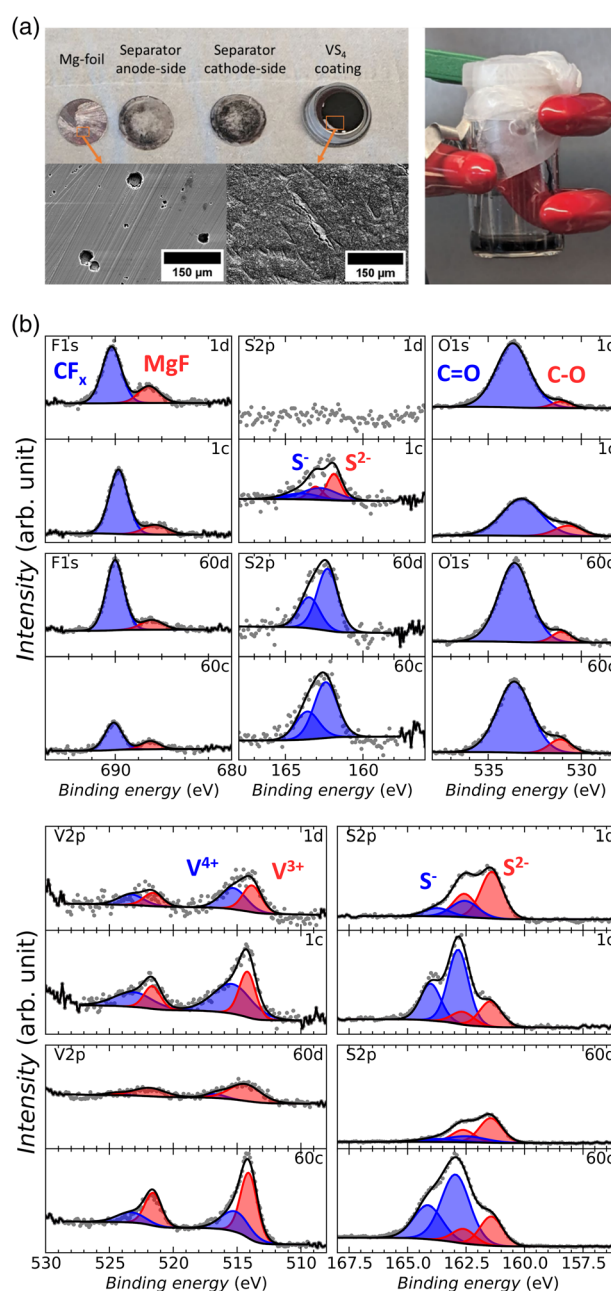
Figure 5. a, left) Photos of a disassembled coin cell after resting conditions for 500 h with the corresponding SEM images showing pit corrosion/dissolution on the anode side and crack formation of the coating on the cathode side. a, right) The discolored electrolyte of a flooded cell is shown after multiple cycles on the right photo. Ex situ XPS measurements of the b, top) magnesium anode and b, bottom) the VS_4 cathode are displayed after 1 and 60 cycles at charged and discharged conditions.

bond cleavage of the VS_4 material, "chopping" the VS_4 chains to a shorter size, resulting in the observed pulverization. The material then becomes amorphous as the crystallinity is slowly lost, which could be confirmed by the broadening and intensity loss of the VS_4 reflexes of XRD measurements investigating cycled samples of the cathode material.

**ADVANCED
SCIENCE NEWS**

www.advancedsciencenews.com

**small
structures**

www.small-structures.com

The pulverized VS_4 then cannot maintain a connection to the binder and current collector, dispersing through the electrolyte toward the anode. To exclude simple binder failure, we additionally tested multiple binder systems. Tested were PVDF coated with NMP (PVDF/NMP), CMC binder with styrene rubber (CMC/SBR), sodium metasilicate, and PVP. However, all of them showed the same behavior which could either mean that the volume expansion of the material is too large, thus releasing the whole particle requiring highly elastic binders for mitigation, or that the root cause is the proposed pulverization which cannot be accommodated by simple binder substitution.

Surface analysis of cycled electrodes by XPS is shown in Figure 5b for the magnesium anode (top) and the VS_4 cathode (bottom). Fitting of the F1s signals revealed partial decomposition of the $Mg[B(hfip)_4]_2$ electrolyte by the formation of Mg-CF$_x$ species (690 eV) and MgF (686 eV) on the magnesium surface from the first discharge onward. This is also supported by the O1s spectra as it showed C—O (533 eV) and C=O (531 eV) bonds, which would be expected as decomposition products of the organic electrolyte. MgO was not observed (expected $\approx$529 eV) which could be either related to a successful removal by scalpel scratching or the formation of a thick decomposition layer, similar to the report by Gao et al., suppressing signals of the underlying layers.[53] The S2p spectra showed no sulfur species on the magnesium surface for the initial discharge. From the first charge onward, the fitted doublets revealed the appearance of S^- (162.8 and 164 eV) and S^{2-} (161.5 and 162.7 eV). Extended cycling showed the formation of MgS$_x$ for both, the charged and discharged conditions indicating some parasitic reaction after the initial discharge. This observation is similar to reports of other sulfur cathodes that have to deal with polysulfide shuttle.[53–55] The initial insertion of cations into the cathode host material leads to the formation of species that are able to dissolve or disperse into the electrolyte upon the sequential charge. They can then travel toward the anode reacting and passivating it. In the case of VS_4, this could happen if the inserted magnesium led to dissociation of the sulfur-vanadium or the sulfur–sulfur bonds, which are then not successfully reformed at the charging step when magnesium is removed from the host lattice. The broken bonds could therefore lead to smaller (un-)charged VS_4 clusters causing dispersion and pulverization of the material or lead to the formation of short polysulfides (S_2^{2-}), dissolving into the electrolyte. As the latter could not be detected by Raman measurements, we assume that mostly pulverization of the material occurs. The loss of active material can be directly connected to the strong capacity fading of the cell. The low Coulombic efficiency of only $\approx$90% can be explained by the parasitic reactions that occur. This includes the pulverization and dispersion of VS_4 leading to active material loss on the cathode side, as well as reactions of the electrolyte and the VS_4 clusters on the magnesium surface, forming MgS, MgF$_2$, and other subspecies.

XPS measurements of the cathode revealed mixed oxidation states of vanadium. The discharged samples showed a shift toward vanadium +III (514.2 and 521.6 eV), which is reversibly oxidized to +IV (515.4 and 523.1 eV) as also seen for the prolonged cycled samples. The S 2p spectra could be successfully fitted with two doublets for S^- and S^{2-}. Upon discharge, the S^{2-} species dominated while for the charged condition mostly S^- is observed. As this redox process also appeared for the

sample that was cycled for 60 times, it seemed highly reversible and is in good agreement with the proposed mechanisms that attribute magnesium insertion with an accompanied bond disassociation of the disulfide S_2^{2-} group forming 2 S^{2-}.[20,24,28]

XPS measurements confirmed the SCAR mechanism as reversible redox behavior of the vanadium and sulfur species could be observed. However, the formation MgCF$_x$, MgF$_2$, and MgS$_x$ indicates severe passivation of the magnesium anode. Especially the MgS$_x$ component also hints toward parasitic reactions of VS_4, such as slight dissolution or pulverization of material into the electrolyte.

Figure 6a shows the XANES results of ex situ measured VS_4 electrode samples, charged (2.7 V) and discharged (0.01 V) for 1 and 5 cycles in comparison with a fresh electrode kept at OCV for $\approx$20 h. A reversible oxidation–reduction evolution was observed for both S and V. In comparison, the OCV sample showed similar XANES features to the discharged samples in both cases. This supports a self-discharge behavior for longer OCV times. Distinct intensity (S) and edge energy shifts could be monitored between the charged and discharged samples. The evolution in the V pre-edge peaks and edge features suggested a gradual local distortion along with the V redox. In case of the S spectra, a reduction of the S_2^{2-} position ($\approx$2471 eV) and an increased splitting at discharge condition were identified. In comparison with the CaSO$_4$ reference, a reversible formation of a S^{4+} species was observed that completely vanishes upon discharge. This might be related to an electrolyte interaction with the active material forming sulfates during charging conditions indicating some unexplored side reactions.

To quantify the evolutions in S K-edge XANES, a deconvolution was performed (Figure 6b,d) using five Pseudo-Voigt peak functions and two arctangent step functions as background representing the transition of the ejected photoelectron to the continuum.[56,57] In this approach, the measured VS_4 electrodes were treated as a mixture of different sulfur species and each Pseudo-Voigt function implied their respective $1s \rightarrow 3p$ transition, while one-step function represented the transitions to the continuum for unoxidized S forms and the other for the oxidized form.[58] To enable the fitting, the Pseudo-Voigt functions were fixed as 50% Gaussian +50% Lorentzian, and their widths were held for 1.2 eV for the first four peaks (pv1–pv4), and the width of arctangent step functions was also constrained to be 1.1 eV, as suggested in the literature.[58]

The peak energy (centroid) and area (amplitude) of the most prominent S whitelines (pv1) showed a linear relationship with the oxidation state of the S atom.[47] However, due to the noise and broadening, the peaks were poorly resolved and therefore cannot be simply assigned to individual S oxidation states (-2, -1, 0, $+4$, $+6$). Nevertheless, a general agreement in the evolution of $s \rightarrow p$ transition energy (centroid) and the content of available vacant p levels (amplitude) between charged and discharged states evidenced the S redox in these initial cycles. The V K-edge pre-edge peaks demonstrated the same evolution (Figure 6c,e), as indicated by the g1 and g2 Gaussian peaks, representing the V redox. As both, the V and S XANES showed reversible behavior in the initial cycles and are in agreement with the XPS and the calculated DOS results, this supports the proposed insertion mechanism of SCAR materials that feature a simultaneous anionic and cationic oxidation/reduction.
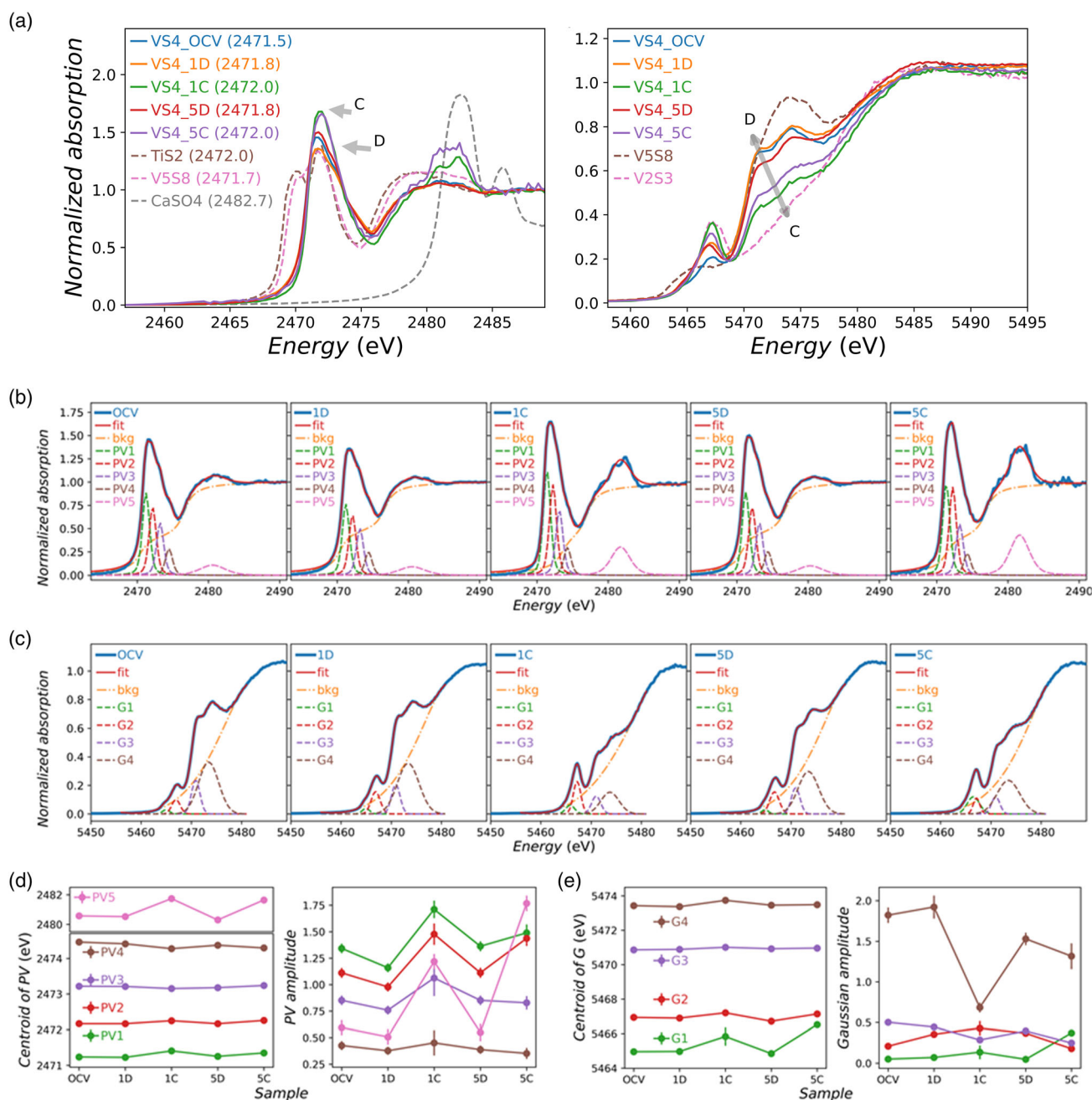
Figure 6. Normalized S and V K-edge XANES a) of ex situ measured VS_4 electrodes at OCV and at charged (C, 2.7 V) and discharged (D, 0.01 V) states for 1 and 5 cycles. Dashed lines represent spectra from reference standards. Deconvolution b) of the S K-edge XANES of VS_4 electrode from OCV and the first and fifth charged (C) and discharged (D) states, by using two arctangent step functions as background (bkg) with five Pseudo-Voigt (PV) peak functions. The V K-edge XANES pre-edge fitting c) was performed using a linear + Lorentzian background (bkg) with 4 Gaussian (G1–G4) peak functions; d) shows the fitted Pseudo-Voigt peaks energy (centroid) and area (pv amplitude) for S while e) displays the fitted Gaussian peaks energy (centroid) and area (Gaussian amplitude) for V.

3. Conclusion

A scalable solid-state reaction for the generation of phase-pure, micron-sized VS_4 particles was successfully step-wise refined. Thereby, the ball milling mixing step was identified to have the biggest impact on the final product purity. An optimized synthesis is achieved for a 1:6 vanadium to sulfur ratio at a ball milling speed of 750 rpm for 5 h and a heating step at 400 °C for at least 48 h. Postprocessing by wet milling and a CS_2 wash of the product helped to reduce agglomeration and removed unreacted S_8, leading to reliable electrochemical performance. Characterization of the micron-sized VS_4 needles was in good

agreement with previous literature confirming a successful synthesis. The established synthetic protocol also allows modification of the VS_4 structure by elemental doping for further exploring the SCAR chemistry.

Electrochemical test showed that the micron-sized VS_4 cathode was able to deliver a capacity (420 mAh g^{-1}) close to the theoretical value at 0.1 C, indicating fairly good reaction kinetics and high energy. However, fast capacity decay and severe overcharging were evident, which could be alleviated by using electrolytes with highe concentration (0.5 M) and higher viscosity (G2). To this end, a longer cycle life of 300 cycles was achieved with CE reaching 94%. Mechanistic investigations revealed reversible oxidation and reduction of both, the sulfur and vanadium species, supporting the SCAR insertion mechanism. However, degradation is evident and most likely triggered by pulverization and leaching of active material into the electrolyte/separator, leading to parasitic reactions on the anode. Future work should address this issue by strategies to avoid active material loss, e.g., using tailored binders that maintain a better adhesion to the active material by cross-polymerization or lower intrinsic Young's modulus, a coating of the VS_4 particles to physically protect the active material from leaching into the electrolyte, or the creation of anchoring sites by the introduction of dopants into the VS_4 structure.

4. Experimental Section

Materials: All chemicals used within this publication are listed in Table S2, Supporting Information. The chemical entries are sorted according to the field of use.

Synthesis: All steps prior to sealing the ampoule were carried out in an MBraun glove box with water and oxygen values below 0.1 ppm. After heat treatment, the materials were handled in air atmosphere. The solid-state synthesis of VS_4 was performed similar to previous literature.[39,59,60] To reduce the reaction time from either 10 days or reopening of the ampoule for a secondary mixing step, the heat treatment time was accelerated by mixing of the precursors in a ball mill. Two grams of precursors with desired molar ratio was premixed within a vial by hand and subsequently transferred to a 45 mL Si_3N_4 ball mill jar containing eighteen 10 mm balls (30.6 g, 1:15 powder-to-ball ratio). After ball milling (Fritsch P7 premium line), the powder was scraped from the jar and filled in a borosilicate ampoule with a long funnel. The ampoule is then temporarily sealed, removed from the glove box, and connected to a Schlenk apparatus. After cleaning the Schlenk-system from residual air by three times alternation of argon and vacuum (10^{-3} mbar), the ampoule was melt sealed under vacuum by a flame torch. The ampoules were then placed in alumina crucibles and heat-treated. The respective heating/cooling rates were set to 100 K h^{-1}. After reaching 298 K, the ampoules were removed from the muffle furnace, opened with a glass cutter, and the material was coarsely ground with mortar and pistil. For further reduction of particle size, 0.5 g of material was transferred to a 20 mL ZrO_2 ball mill jar containing five 10 mm balls (14.9 g, 1:30 powder to ball ratio). After milling (Fritsch P7 premium line), the powder was scraped from the jar and further purified. For wet milling, 3 g of isopropanol was added as a dispersion agent. After milling, the product was rinsed from the jar with more isopropanol and the solvent was evaporated by storing the dispersion in a petri dish at room temperature overnight in the fume hood. The obtained powder was further purified. For purification, the powder was washed three times with carbon disulfide to remove residual sulfur. In the perspective of scale up attempts, this step could easily be replaced by sulfur removal under reduced pressure and elevated temperatures as reported in prior solid-state studies of VS_4.[39,59] All products and their respective synthesis parameters can be found in the supporting information (Table S3, Supporting Information).

Slurry Preparation and Coating: Cathode slurries were prepared in a composition of 70 wt% active material, 20 wt% Super P carbon, and 10 wt% binder consisting of 5 wt% SBR and 5 wt% sodium CMC. For the binder, 2 wt% aqueous CMC stock solution and 5 wt% aqueous SBR stock dispersion were used. For 100 mg composition, 500 mg water and 75 mg isopropanol (IprOH) have to be added to achieve the correct consistency and good dispersibility. In the case of the PVP binder, 2.5 wt% stock solutions with ethanol were used. The components were then mixed with a planetary centrifugal mixer (Thinky ARE-250) at 1500 rpm for 10 min followed by a defoaming step at 400 rpm for 5 min. The mixing procedure was repeated three times. Coating was performed on bare aluminum foil with a doctor blade coater. A coating height of 100–150 µm and a speed of 10 mm s^{-1} were used, resulting in mass loadings of ≈1 mg cm^{-2}. The coating was dried in the fume hood at room temperature overnight. After punching 12 mm discs from the cathode coating, a second drying step under vacuum at 10^{-3} mbar and 353 K (80 °C) was applied overnight prior to transfer in the glove box.

Cell Preparation: All cell components were dried thoroughly before transferred in the glove box. The oxide surface of the magnesium anode disc was removed by scraping with a scalpel prior to the cell assembly. Coin cells were assembled using a 14 mm magnesium anode, a 16 mm glass fiber separator (Whatman GF/C), and an 11.8 mm cathode (≈1 cm^2). About 60 µL 0.3 M $Mg(B[hfip]_4)_2$.3DME in DME was used as an electrolyte. Preparation of the electrolyte was performed according to literature and prior to use tested for purity (^1H NMR, Figure S14, Supporting Information).[54] All cells were crimped at a pressure of 0.7 t. Degradation studies were performed using galvanostatic charging with potential limitation protocols at a Biologic BCS 805 potentiostat and applied currents of 50 mA g^{-1} with respect to the cathode active material (VS_4).

Computational Details: Periodic DFT calculations were employed to study the electronic structure of VS_4.[61,62] The projector-augmented wave method was used as implemented in the Vienna ab initio simulation package (VASP).[63–66] The strongly constrained and appropriately normed exchange–correlation functional was combined with the revised Vydrov–van Voorhis (rVV10) nonlocal correlation functional to additionally account for dispersion interactions between the VS_4 strands.[67–69] The plane wave cutoff was set to 520 eV, and an electronic convergence criterion of 1×10^{-6} eV was employed. A supercell containing 8 formula units was assumed, and all structures were relaxed without restrictions until the forces converged below 0.01 eV Å^{-1}, while the Brillouin zone was sampled using a $2 \times 3 \times 4$k-point mesh. For the simulations of X-ray absorption spectroscopy (XAS) spectra, the XCH method was used as implemented in VASP, and convergence with respect to the cutoff of the plane wave basis set, the k-point mesh, the number of unoccupied bands, and the supercell size was tested.[70–73]

XRD/PDF Analysis: All samples were measured in Debye–Scherrer mode at a Stoe Stadi P powder diffractometer equipped with an IP-PSD Mythen 2K detector. Monochromatized Ag-K$_{\alpha1}$ ($\lambda = 0.55941$ Å) radiation was obtained by a curved Ge(111) surface. The X-ray tube was operated at 40 kV/40 mA. A LaB$_6$ reference (NIST660b) was utilized to account for instrumental contributions and alignment. In the case of pair distribution function measurements, additional ranges were measured for higher 2-theta to counteract the lower intensities, achieving better signal to noise ratios.

DLS: All samples were measured three times using a Mastersizer 3000 + Ultra and afterwards averaged. Each measurement was performed by adding one spatula of powder to isopropanol as dispersion media. After ultrasonification for 2 min (at 70% intensity, then switched off), the measurement was started.

SEM/EDX: SEM measurements were performed using a Thermo Scientific Apreo 2 equipped with an Ultra-Dry EDX detector. For SEM imaging, a voltage of 20 kV and a current of 13 nA were used. EDX mappings were recorded with a map resolution of 768×512 pixels, a frame time of 30 s, and a dwell time of 76.30 µs, utilizing the same voltage and current parameters as for the SEM images.

Raman: Raman measurements were performed at a Renishaw inVia confocal Raman microscope using a green 532 nm laser with 1800 l mm^{-1} grating and an exposure time of 30 s for 4 accumulations. Prior instrument calibration was performed using a silicon wafer.

FT-IR: Measurements were performed using a PerkinElmer Spectrum Two instrument in UATR mode equipped with a MIR TGS detector and a KBr beam splitter. The sample was accumulated for a set resolution of 4 over 8 scans.

XAS: XAS was performed at the Phoenix beamline of the Swiss Light source (PSI, Switzerland) to study the cationic and anionic redox behavior of VS_4-based electrodes within the initial cycles. Pristine VS_4 and reference standards (V_2S_3, V_5S_8, $CaSO_4$, VO, V_2O_3, VO_2, and V_2O_5) were prepared as pellet samples diluted with cellulose. Cycled electrodes were extracted from disassembled cells that were galvanostatically charged/discharged to 2.7/0.1 V at 50 mA g^{-1} to the respective cycle; then the extracted electrode tapes were washed with DME and dried. All samples were sealed inside an Ar-filled glove box using Kapton tapes on the bottom and 8 μm Kapton foils on top to receive the incident beam, which was further attached to Cu samples plates with carbon tapes. The prepared samples and holders were transported to the beamline in air-tight containers. Before the XAS measurements, the Cu plates were taken out of the glove box and inserted into the vacuum chamber. S and V K-edge absorption spectra were collected under a vacuum of 10^{-5} mbar in total fluorescence yield mode using a solid-state detector (Ketek GmBH) with 150 eV energy resolution.

The obtained absorption spectra were further analyzed with Larch software.[74] The S absorption spectra were calibrated with a +1 eV energy shift based on the white line of $CaSO_4$ (2481.5 eV) with respect to the one in the ESRF database (2482.5 eV).[75] Normalization was performed by regressing a quadratic polynomial to the data before and after the edge step, then subtracting the pre-edge polynomial from the spectra and dividing it by the edge jump. Normalized S K-edge absorption spectra were deconvoluted into five Pseudo-Voigt peaks with two arctangent step functions as background using the LMFIT package.[76] The pre-edge peaks and shoulder features of V K-edge absorption spectra were also fitted through a linear + Lorentzian background and four Gaussian peak functions.

XPS: XPS was recorded under high vacuum conditions using a near-ambient pressure XPS (NAP-XPS) system EnviroESCA from Specs equipped with an Al-Kα source (1486.71 eV) operated at 15 kV, 43 W (3 mA emission) and a Phoibos 150 NAP hemispherical analyzer. The base pressure was 10^{-7} mbar in the analysis chamber and 10^{-9} mbar in the analyzer section. High-resolution spectra were recorded using a pass energy of 30 eV. Peak fitting was performed with CasaXPS, version 2.3.25P R1.0, using a Shirley-type background and 70% Gaussian and 30% Lorentzian profiles.[77]

Research Data Management: Research data were organized within an electronic Jupyter lab notebook and uploaded to a Kadi4mat instance.[78] Publishing of the research data was performed by a Kadi4mat integration of Zenodo.[79] All research data produced within this work are publicly available at 10.5281/zenodo.10985810 following the FAIR guidelines.

Supporting Information

Supporting Information is available from the Wiley Online Library or from the author.

Conflict of Interest

The authors declare no conflict of interest.

Author Contributions

Adam Reupert: conceptualization (supporting); formal analysis (equal); investigation (lead); methodology (lead); validation (lead); writing—original draft (lead). **Hanna Schleicher**: data curation (supporting); formal analysis (supporting); investigation (supporting); writing—review and editing (supporting). **Yang Hu**: data curation (equal); formal analysis (equal); investigation (equal); methodology (equal); validation (equal); writing—review and editing (equal). **Stefan Fuchs**: formal analysis (equal); investigation (equal); methodology (equal). **Manuel Dillenz**: data curation (supporting); formal analysis (supporting); investigation (supporting); methodology (supporting); writing—review and editing (equal). **Camelia N. Borca**: formal analysis (supporting); investigation (supporting); methodology (supporting); writing—review and editing (equal). **Thomas Huthwelker**: formal analysis (supporting); investigation (supporting); resources (supporting); writing—review and editing (supporting). **Axel Groß**: formal analysis (supporting); resources (supporting); supervision (supporting); writing—review and editing (equal). **Maximilian Fichtner**: funding acquisition (supporting); resources (lead); supervision (supporting); writing—review and editing (equal). **Zhenyou Li**: conceptualization (lead); funding acquisition (lead); project administration (lead); supervision (lead); writing—review and editing (equal).

Data Availability Statement

The data that support the findings of this study are openly available in Zenodo at https://doi.org/10.5281/zenodo.10985810, reference number 10985810.

[1] Passenger Cars - Worldwide | Statista Market Forecast, https://www.statista.com/outlook/mmo/passenger-cars/worldwide (accessed: February 2024).

[2] Renewables consumption worldwide 2050, https://www.statista.com/statistics/218316/renewable-energy-consumption-worldwide/ (accessed: February 2024).

[3] European Commission. Directorate General for Internal Market, Industry, Entrepreneurship and SMEs., Study on the critical raw materials for the EU 2023: final report., Publications Office, LU, 2023.

[4] Y. Tian, G. Zeng, A. Rutt, T. Shi, H. Kim, J. Wang, J. Koettgen, Y. Sun, B. Ouyang, T. Chen, Z. Lun, Z. Rong, K. Persson, G. Ceder, *Chem. Rev.* **2021**, *121*, 1623.

[5] Y. Liang, H. Dong, D. Aurbach, Y. Yao, *Nat. Energy* **2020**, *5*, 646.

[6] M. Jäckle, A. Groß, *J. Chem. Phys.* **2014**, *141*, 174710.

[7] R. D. Shannon, *Acta Cryst. A* **1976**, *32*, 751.

[8] A. Roy, M. Sotoudeh, S. Dinda, Y. Tang, C. Kübel, A. Groß, Z. Zhao-Karger, M. Fichtner, Z. Li, *Nat. Commun.* **2024**, *15*, 492.

[9] K. Taniguchi, Y. Gu, Y. Katsura, T. Yoshino, H. Takagi, *Appl. Phys. Express* **2016**, *9*, 011801.

[10] M. Mao, X. Ji, S. Hou, T. Gao, F. Wang, L. Chen, X. Fan, J. Chen, J. Ma, C. Wang, *Chem. Mater.* **2019**, *31*, 3183.

[11] L. E. Blanc, X. Sun, A. Shyamsunder, V. Duffort, L. F. Nazar, *Small Methods* **2020**, *4*, 2000029.

[12] J. A. Blázquez, R. R. Maça, O. Leonet, E. Azaceta, A. Mukherjee, Z. Zhao-Karger, Z. Li, A. Kovalevsky, A. Fernández-Barquín, A. R. Mainar, P. Jankowski, L. Rademacher, S. Dey, S. E. Dutton, C. P. Grey, J. Drews, J. Häcker, T. Danner, A. Latz, D. Sotta, M. R. Palacin, J.-F. Martin, J. M. G. Lastra, M. Fichtner, S. Kundu, A. Kraytsberg, Y. Ein-Eli, M. Noked, D. Aurbach, *Energy Environ. Sci.* **2023**, *16*, 1964.

[13] R. Mohtadi, O. Tutusaus, T. S. Arthur, Z. Zhao-Karger, M. Fichtner, *Joule* **2021**, *5*, 581.

[14] Z. Li, J. Häcker, M. Fichtner, Z. Zhao-Karger, *Adv. Energy Mater.* **2023**, *13*, 2300682.

[15] S.-K. Jung, K. Kang, *Nat. Energy* **2017**, *2*, 912.

[16] M. Mao, Y. Tong, Q. Zhang, Y.-S. Hu, H. Li, X. Huang, L. Chen, L. Gu, L. Suo, *Nano Lett.* **2020**, *20*, 6852.

[17] K. Taniguchi, T. Yoshino, Y. Gu, Y. Katsura, H. Takagi, *J. Electrochem. Soc.* **2015**, *162*, A198.

[18] M. Mao, C. Yang, Z. Lin, Y. Tong, Q. Zhang, L. Gu, L. Hong, L. Suo, Y.-S. Hu, H. Li, X. Huang, L. Chen, *JACS Au* **2021**, *1*, 1266.

[19] Y. Gu, Y. Katsura, T. Yoshino, H. Takagi, K. Taniguchi, *Sci. Rep.* **2015**, *5*, 12486.

[20] S. Dey, J. Lee, S. Britto, J. M. Stratford, E. N. Keyzer, M. T. Dunstan, G. Cibin, S. J. Cassidy, M. Elgaml, C. P. Grey, *J. Am. Chem. Soc.* **2020**, *142*, 19588.

[21] S. Ding, B. Zhou, C. Chen, Z. Huang, P. Li, S. Wang, G. Cao, M. Zhang, *Nano-Micro Lett.* **2020**, *12*, 39.

[22] K. Shimoda, K. Kuratani, S. Kobayashi, T. Takeuchi, M. Murakami, A. Kuwabara, H. Sakaebe, *ACS Appl. Mater. Interfaces* **2022**, *14*, 33191.

[23] K. Shimoda, K. Koganei, T. Takeuchi, T. Matsunaga, M. Murakami, H. Sakaebe, H. Kobayashi, E. Matsubara, *RSC Adv.* **2019**, *9*, 23979.

[24] Z. Li, B. P. Vinayan, P. Jankowski, C. Njel, A. Roy, T. Vegge, J. Maibach, J. M. G. Lastra, M. Fichtner, Z. Zhao-Karger, *Angew. Chem. Int. Ed.* **2020**, *59*, 11483.

[25] T. Pavčnik, M. Lozinšek, K. Pirnat, A. Vizintin, T. Mandai, D. Aurbach, R. Dominko, J. Bitenc, *ACS Appl. Mater. Interfaces* **2022**, *14*, 26766.

[26] Y.-Y. Liu, L. Xu, X.-T. Guo, T.-T. Lv, H. Pang, *J. Mater. Chem. A* **2020**, *8*, 20781.

[27] Z. Qin, Y. Hu, C. Lv, S. Yao, G. Chen, *Chem. Eng. J.* **2022**, *433*, 133765.

[28] P. Jankowski, J. M. G. Lastra, *J. Energy Storage* **2023**, *62*, 106895.

[29] Y. Wang, Z. Liu, C. Wang, X. Yi, R. Chen, L. Ma, Y. Hu, G. Zhu, T. Chen, Z. Tie, J. Ma, J. Liu, Z. Jin, *Adv. Mater.* **2018**, *30*, 1802563.

[30] J. Zhu, X. Zhang, H. Gao, Y. Shao, Y. Liu, Y. Zhu, J. Zhang, L. Ji, *J. Power Sources* **2022**, *518*, 230731.

[31] P. Jing, H. Lu, W. Yang, Y. Cao, B. Xu, W. Cai, Y. Deng, *Ionics* **2020**, *26*, 777.

[32] J. Li, Y. Xu, Y. He, Z. Zhang, C. Zhu, X. Zhou, *J. Phys. Chem. Lett.* **2022**, *13*, 5726.

[33] Y. Wang, C. Wang, X. Yi, Y. Hu, L. Wang, L. Ma, G. Zhu, T. Chen, Z. Jin, *Energy Storage Mater.* **2019**, *23*, 741.

[34] S. Ding, Z. Li, X. Dai, C. Sun, A. Meng, *Chem. Eng. J.* **2021**, *417*, 129328.

[35] Y. Umemura, T. Takeuchi, H. Sakaebe, H. Kiuchi, T. Yaji, M. Katayama, *Electrochemistry* **2021**, *89*, 273.

[36] Z. Li, S. Ding, J. Yin, M. Zhang, C. Sun, A. Meng, *J. Power Sources* **2020**, *451*, 227815.

[37] M. R. Palacin, P. Johansson, R. Dominko, B. Dlugatch, D. Aurbach, Z. Li, M. Fichtner, O. Lužanin, J. Bitenc, Z. Wei, C. Glaser, J. Janek, A. Fernández-Barquín, A. R. Mainar, O. Leonet, I. Urdampilleta, J. A. Blázquez, D. S. Tchitchekova, A. Ponrouch, P. Canepa, G. S. Gautam, R. S. R. G. Casilda, C. S. Martinez-Cisneros, N. U. Torres, A. Varez, J.-Y. Sanchez, K. V. Kravchyk, M. V. Kovalenko, A. A. Teck, H. Shiel, I. E. L. Stephens, M. P. Ryan, E. Zemlyanushin, S. Dsoke, R. Grieco, N. Patil, R. Marcilla, X. Gao, C. J. Carmalt, G. He, M.-M. Titirici, *J. Phys. Energy* **2024**, *6*, 031501.

[38] M. Yokoyama, M. Yoshimura, M. Wakihara, S. Somiya, M. Taniguchi, *J. Solid State Chem.* **1985**, *60*, 182.

[39] M. N. Kozlova, Y. V. Mironov, E. D. Grayfer, A. I. Smolentsev, V. I. Zaikovskii, N. A. Nebogatikova, T. Y. Podlipskaya, V. E. Fedorov, *Chem. – Eur. J.* **2015**, *21*, 4639.

[40] H. M. P., A. Chandra Bose, *Energy Fuels* **2023**, *37*, 10799.

[41] M. S. Weimer, R. F. McCarthy, J. D. Emery, M. J. Bedzyk, F. G. Sen, A. Kinaci, M. K. Y. Chan, A. S. Hock, A. B. F. Martinson, *Chem. Mater.* **2017**, *29*, 2864.

[42] M. B. Mitchell, V. N. Sheinker, M. G. White, *J. Phys. Chem.* **1996**, *100*, 7550.

[43] J. Sun, Y. Liu, J. Deng, L. Jing, M. Bao, Q. Sun, L. Li, L. Wu, X. Hao, H. Dai, *Catalysts* **2022**, *12*, 1302.

[44] W. Li, J. Huang, L. Feng, L. Cao, Y. Feng, H. Wang, J. Li, C. Yao, *J. Mater. Chem. A* **2017**, *5*, 20217.

[45] L. Yu, S.-X. Zhao, Q. Wu, J.-W. Zhao, G. Wei, *Adv. Funct. Mater.* **2020**, *30*, 2000427.

[46] G. Lui, G. Jiang, A. Duan, J. Broughton, J. Zhang, M. W. Fowler, A. Yu, *Ind. Eng. Chem. Res.* **2015**, *54*, 2682.

[47] A. Vairavamurthy, *Spectrochim. Acta Part A* **1998**, *54*, 2009.

[48] L. Zhang, D. Sun, J. Kang, H.-T. Wang, S.-H. Hsieh, W.-F. Pong, H. A. Bechtel, J. Feng, L.-W. Wang, E. J. Cairns, J. Guo, *Nano Lett.* **2018**, *18*, 4506.

[49] D. T. Pham, B. Sambandam, S. Kim, J. Jo, S. Kim, S. Park, V. Mathew, Y.-K. Sun, K. Kim, J. Kim, *Energy Storage Mater.* **2019**, *19*, 270.

[50] Q. Pang, Y. Zhao, Y. Yu, X. Bian, X. Wang, Y. Wei, Y. Gao, G. Chen, *ChemSusChem* **2018**, *11*, 735.

[51] Y. Liu, Y. Elias, J. Meng, D. Aurbach, R. Zou, D. Xia, Q. Pang, *Joule* **2021**, *5*, 2323.

[52] S. Wang, H. Chen, J. Liao, Q. Sun, F. Zhao, J. Luo, X. Lin, X. Niu, M. Wu, R. Li, X. Sun, *ACS Energy Lett.* **2019**, *4*, 755.

[53] T. Gao, S. Hou, K. Huynh, F. Wang, N. Eidson, X. Fan, F. Han, C. Luo, M. Mao, X. Li, C. Wang, *ACS Appl. Mater. Interfaces* **2018**, *10*, 14767.

[54] Z. Zhao-Karger, R. Liu, W. Dai, Z. Li, T. Diemant, B. P. Vinayan, C. Bonatto Minella, X. Yu, A. Manthiram, R. J. Behm, M. Ruben, M. Fichtner, *ACS Energy Lett.* **2018**, *3*, 2005.

[55] J. Häcker, C. Danner, B. Sievert, I. Biswas, Z. Zhao-Karger, N. Wagner, K. A. Friedrich, *Electrochim. Acta* **2020**, *338*, 135787.

[56] L. J. Kubeneck, L. Notini, K. A. Rothwell, G. Fantappiè, T. Huthwelker, L. K. ThomasArrigo, R. Kretzschmar, *Geochim. Cosmochim. Acta* **2024**, *370*, 173.

[57] R. F. Costa, R. F. Firmano, M. Colzato, C. A. C. Crusciol, L. R. F. Alleoni, *Geoderma* **2022**, *406*, 115461.

[58] G. P. Huffman, S. Mitra, F. E. Huggins, N. Shah, S. Vaidya, F. Lu, *Energy Fuels* **1991**, *5*, 574.

[59] K. Koganei, A. Sakuda, T. Takeuchi, H. Sakaebe, H. Kobayashi, H. Kageyama, T. Kawaguchi, H. Kiuchi, K. Nakanishi, M. Yoshimura, T. Ohta, T. Fukunaga, E. Matsubara, *Solid State Ionics* **2018**, *323*, 32.

ADVANCED
SCIENCE NEWS

www.advancedsciencenews.com

small
structures

www.small-structures.com

[60] E. Flores, E. Muñoz-Cortés, J. Bodega, O. Caballero-Calero, M. Martín-González, C. Sánchez, J. R. Ares, I. J. Ferrer, *ACS Appl. Energy Mater.* **2018**, *1*, 2333.

[61] P. Hohenberg, W. Kohn, *Phys. Rev.* **1964**, *136*, B864.

[62] W. Kohn, L. J. Sham, *Phys. Rev.* **1965**, *140*, A1133.

[63] P. E. Blöchl, *Phys. Rev. B* **1994**, *50*, 17953.

[64] G. Kresse, J. Hafner, *Phys. Rev. B* **1993**, *47*, 558.

[65] G. Kresse, J. Furthmüller, *Phys. Rev. B* **1996**, *54*, 11169.

[66] G. Kresse, D. Joubert, *Phys. Rev. B* **1999**, *59*, 1758.

[67] J. Sun, A. Ruzsinszky, J. P. Perdew, *Phys. Rev. Lett.* **2015**, *115*, 036402.

[68] R. Sabatini, T. Gorni, S. de Gironcoli, *Phys. Rev. B* **2013**, *87*, 041108.

[69] H. Peng, Z.-H. Yang, J. P. Perdew, J. Sun, *Phys. Rev. X* **2016**, *6*, 041005.

[70] M. Taillefumier, D. Cabaret, A.-M. Flank, F. Mauri, *Phys. Rev. B* **2002**, *66*, 195107.

[71] D. Prendergast, G. Galli, *Phys. Rev. Lett.* **2006**, *96*, 215502.

[72] C. Gougoussis, M. Calandra, A. P. Seitsonen, F. Mauri, *Phys. Rev. B* **2009**, *80*, 075102.

[73] F. Karsai, M. Humer, E. Flage-Larsen, P. Blaha, G. Kresse, *Phys. Rev. B* **2018**, *98*, 235205.

[74] M. Newville, *J. Phys.: Conf. Ser.* **2013**, *430*, 012007.

[75] Database Inornagic sulfur compounds, https://www.esrf.fr/home/UsersAndScience/Experiments/XNP/ID21/php/Database-SCompounds.html (accessed: May 2024).

[76] M. Newville, R. Otten, A. Nelson, T. Stensitzki, A. Ingargiola, D. Allan, A. Fox, F. Carter, M. Ray Osborn, D. Pustakhod, S. Weigand, A. Aristov, G. Mark, C. Deil, A. L. R. Hansen, G. Pasquevich, L. Foks, N. Zobrist, O. Frost, S. J.-C. Jaskula, S. Caldwell, P. Eendebak, M. Pompili, J. H. Nielsen, A. Persaud, Lmfit/Lmfit-Py: 1.2.1, Zenodo **2023** (accessed: January 2024).

[77] N. Fairley, V. Fernandez, M. Richard-Plouet, C. Guillot-Deudon, J. Walton, E. Smith, D. Flahaut, M. Greiner, M. Biesinger, S. Tougaard, D. Morgan, J. Baltrusaitis, *Appl. Surf. Sci. Adv.* **2021**, *5*, 100112.

[78] N. Brandt, L. Griem, C. Herrmann, E. Schoof, G. Tosato, Y. Zhao, P. Zschumme, M. Selzer, *Data Sci. J.* **2021**, *20*, 8.

[79] European Organization For Nuclear Research, OpenAIRE, https://www.zenodo.org/ (accessed: February 2024).

[80] K. Momma, F. Izumi, *J Appl Cryst* **2011**, *44*, 1272.

[81] J. Rodriguez-Cavajal, *Newsletter* **2001**, *26*, 12.